Flow stimuli reveal ecologically appropriate responses in mouse visual cortex

Luciano Dyballa[a,1], Mahmood S. Hoseini[b,1], Maria C. Dadarlat[b], Steven W. Zucker[a,c], and Michael P. Stryker[b,2]

[a]Department of Computer Science, Yale University, New Haven, CT 06520; [b]Center for Integrative Neuroscience, University of California, San Francisco, CA 94143-0444; and [c]Department of Biomedical Engineering, Yale University, New Haven, CT 06520

Contributed by Michael P. Stryker, September 4, 2018 (sent for review July 5, 2018; reviewed by Lindsey L. Glickfeld and Cristopher M. Niell)

Assessments of the mouse visual system based on spatial-frequency analysis imply that its visual capacity is low, with few neurons responding to spatial frequencies greater than 0.5 cycles per degree. However, visually mediated behaviors, such as prey capture, suggest that the mouse visual system is more precise. We introduce a stimulus class—visual flow patterns—that is more like what the mouse would encounter in the natural world than are sine-wave gratings but is more tractable for analysis than are natural images. We used 128-site silicon microelectrodes to measure the simultaneous responses of single neurons in the primary visual cortex (V1) of alert mice. While holding temporal-frequency content fixed, we explored a class of drifting patterns of black or white dots that have energy only at higher spatial frequencies. These flow stimuli evoke strong visually mediated responses well beyond those predicted by spatial-frequency analysis. Flow responses predominate in higher spatial-frequency ranges (0.15–1.6 cycles per degree), many are orientation or direction selective, and flow responses of many neurons depend strongly on sign of contrast. Many cells exhibit distributed responses across our stimulus ensemble. Together, these results challenge conventional linear approaches to visual processing and expand our understanding of the mouse's visual capacity to behaviorally relevant ranges.

visual cortex | flow movie | mouse | spatial frequency | receptive field

The mouse has become a major model for studying vision because of the genetic, imaging, and molecular tools available (1). Studies have revealed relationships between macroscopic states of the brain and activity in visual cortex [running vs. stationary (2, 3), pupil size and activity (4, 5), and visual interest (e.g., refs. 5–7)]. However, a basic conundrum has arisen: Behaviorally, mice are capable of sharp, visually mediated behaviors (8–10), such as accurate prey capture (11), but when assessed using standard assays, such as spatial-frequency gratings (Fig. 1), the mouse appears to have very poor vision. Although orientation selectivity has been found (12), receptive fields are large [typically $\geq 25(^\circ)^2$] when estimated by spike-triggered averaging, and spatial-frequency tuning is concentrated below 0.08 cycles per degree (cpd). While this motivates the use of gratings at 0.04 cpd in experiments, it raises the question, How does the visual system perform so exquisitely in natural tasks?

We show here that ecologically relevant stimuli can exercise mouse visual cortex in manifold ways. While plaids (13, 14) and random-dot kinematograms (15, 16) are a step beyond gratings, the leap to natural images (e.g., ref. 17) is more common (e.g., refs. 18 and 19). However, natural images are difficult to obtain (20), difficult to control parametrically, and difficult to analyze beyond second order (21).

For a mouse running through a field, the visual display is like a "waterfall" of illuminated material flowing past, with bright- or dark-oriented segments arising from complex photometric events (Fig. 1*A*) (22). This visual metaphor motivates our stimuli. We approximate such patterns with a class of visual flows composed of dots. These are more natural than drifting gratings but can be parametrically controlled in their orientation (content and angle), spatial frequency, and direction of motion. We call them flows because, intuitively, they consist of a field of particles (either dots or dotted-line segments) dropped into a "flowing river." More formally, each dot is displaced along a vector field in space and time and follows a dynamical system (23). When the orientation structure is removed, the flows reduce to random-dot kinematograms; when the temporal structure is removed, the flows reduce to static Glass patterns (24). Thus, they are rich in geometry and, for humans, the perception of such flows differs from strictly aligned patterns (25, 26). Parametric variations in orientation, direction, etc., define an ensemble of stimuli.

We here explore activity in mouse primary visual cortex (V1) in response to the flow ensemble. In many cases flow stimuli elicit more vigorous responses than drifting gratings, particularly at high spatial frequencies 3–5 octaves above 0.04 cpd. Some V1 neurons are classical, resembling feature detectors, while others exhibit a mixed selectivity rarely reported in early visual cortex. The rich ensemble of selectivities in V1 may equip the mouse to behave in the natural world.

Results

Cells in V1 Have Diverse Preferred Stimuli. We developed an ensemble of stimuli including drifting gratings, single-dot flows (random-dot kinematograms), and oriented flows where each element consists of three or four dots (*Materials and Methods*). The stimuli had either positive contrast (bright dots) or negative

Significance

The visual system of the mouse is now widely studied as a model for development and disease in humans. Studies of its primary visual cortex (V1) using conventional grating stimuli to construct linear–nonlinear receptive fields suggest that the mouse must have very poor vision. Using stimuli resembling the flow of images across the retina as the mouse moves through the grass, we find that most V1 neurons respond reliably to very much finer details of the visual scene than previously believed. Our findings suggest that the conventional notion of a unique receptive field does not capture the operation of the neural network in mouse V1.

Author contributions: L.D., M.S.H., S.W.Z., and M.P.S. designed research; M.S.H. and M.C.D. performed research; L.D. and S.W.Z. analyzed data; L.D., M.S.H., S.W.Z., and M.P.S. wrote the paper; L.D. designed and implemented stimuli; and S.W.Z. designed the stimuli.

Reviewers: L.L.G., Duke University; and C.M.N., University of Oregon.

The authors declare no conflict of interest.

Data deposition: Computer code used to generate stimuli has been deposited at https://github.com/zuckerlab/FlowStims.

[1]L.D. and M.S.H. contributed equally to this work.

[2]To whom correspondence should be addressed. Email: stryker@phy.ucsf.edu.

This article contains supporting information online at www.pnas.org/lookup/suppl/doi:10.1073/pnas.1811265115/-/DCSupplemental.

Published online October 16, 2018.

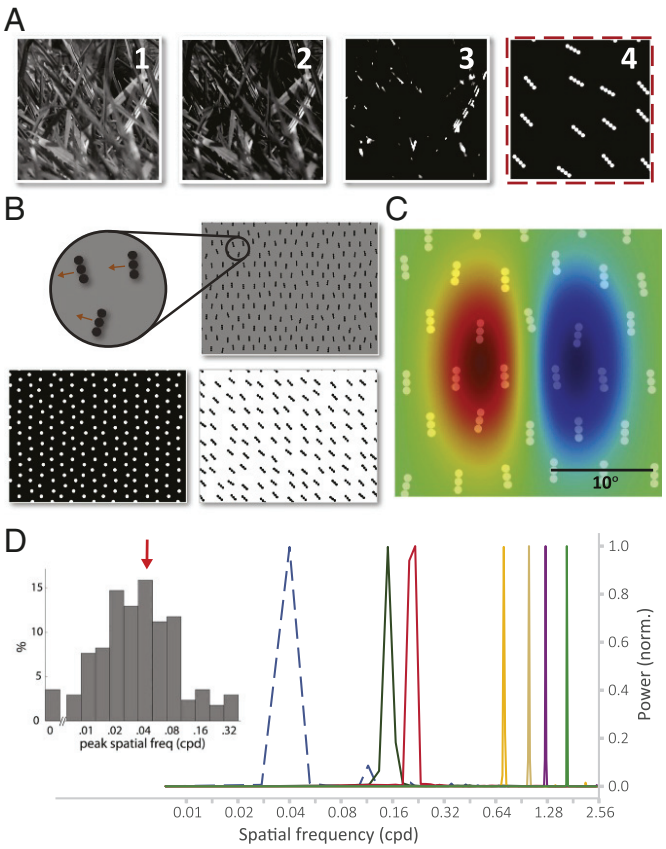

Fig. 1. Introducing flow stimuli. (*A*) Ecological motivation. Working with a single frame (*A*, *1–3*), a grassy patch is modified to emphasize salient higher contrasts. Our abstraction (the flow field in *A*, *4*) approximates this with a binary pattern of random, oriented dotted segments. (*B*) We generalize to flow fields consisting of dotted segments of different lengths, emphasizing two geometries [oriented (three or four aligned dots) or nonoriented (single dots)], two contrast polarities (positive or negative), different contrast magnitudes, and various sizes. The full flow stimulus is a movie of one such flow field, drifting across the screen with small random perturbations to suppress rigidity (*Materials and Methods*) (examples in SI *Appendix*, Movies S1 and S2). (*C*) Flow responses are inconsistent with classical filtering views of V1. Shown is a Gabor receptive field at 0.04 cpd superimposed onto the three-dot flow whose energy peaks at 0.24 cpd (example in *B*, *Top Right*), for comparison. (*D*) The 1D discrete Fourier transforms (single sided) of the flows used in our experiments (peaks at 0.15 cpd, 0.24 cpd, 0.7 cpd, 1.0 cpd, 1.25 cpd, and 1.6 cpd) have power well beyond 0.04 cpd (dashed curve), which is the spatial frequency previously reported as optimal for cells in mouse V1 (compare *D*, *Inset*). Adapted with permission from ref. 12. To compare stimuli, each spectrum is normalized by the power at the peak frequency (norm) (2D spectra in *SI Appendix*, Figs. S14 and S15).

contrast (dark dots). Activity is plotted as an array of peristimulus time histograms (PSTHs) and tuning curves for each unit, to facilitate a quick assessment of the different "dimensions" of a cell's response. Experiments were conducted in two cohorts, the first one with grating stimuli at 0.04 cpd and both grating and flow stimuli at 0.15 cpd and 0.24 cpd and the second cohort with grating stimuli at 0.04 cpd and both grating and flow stimuli at 0.7 cpd, 1.0 cpd, 1.25 cpd, and 1.6 cpd. All stimuli in both cohorts had a fixed temporal frequency of 4 Hz.

We begin with example cells from cohort 1. The first one (Fig. 2*A*) has the response profile one would expect for a simple cell in V1. It responds almost exclusively to low-frequency gratings; the PSTHs for high-frequency gratings and for flows (both one-dot and three-dot elements) remain virtually at baseline. Its spike-triggered average (STA) depicts a classical receptive field, consistent with the frequency response, and it is well tuned for orientation. But such cells were relatively rare in our experiments (discussed below). Another example (Fig. 2*B*) exhibits a weak response to gratings and a stronger response to flows. The STA, which would predict a strong response to low-frequency gratings, completely fails to predict this response profile. Finally, many cells are multidimensional (Fig. 2*C*): They respond well to several stimuli from the ensemble, including gratings and flows at multiple spatial frequencies. Note the diversity in the temporal response profile: a periodic (often interpreted as linear) response to gratings at low spatial frequency; a sustained (interpreted as nonlinear) response to gratings at higher frequencies; and a transient burst of activity to positive, oriented flows. It would be inappropriate to label this cell a classical feature detector. The STA again does not predict the response profile, and the PSTHs reveal different tuning widths and different first-spike latencies, as well as linear vs. nonlinear and transient vs. sustained responses.

Responses to Optimal Flows Span a Wide Range of Spatial Frequencies. To quantify this diversity at the population level, we relaxed the notion of a unique preferred stimulus for a cell to allow for multiple possible preferences, according to the following definitions. While this leads to a crude classification of cell types, we stress that it is merely a set of labels for discussion; the underlying complexity remains in the PSTHs.

An individual stimulus is significant for a particular cell if the average firing rate for that stimulus is significantly higher than that for its preceding interstimulus interval (Mann–Whitney *U* test). A cell prefers a stimulus class (e.g., flows or gratings) if at least one variation of that class (spatial frequency, geometry, or contrast polarity) is significant and has average peak firing rate significantly higher than the peak firing rates of all significant variations of the other class (Kruskal–Wallis rank-sum test, Conover–Iman post hoc, Bonferroni correction, $P < 0.05$). When there is no preferred stimulus class but there are significant stimuli in both classes, we classify the cell as multiclass, or simply *multi*. Thus, the preferred stimulus class, or type of a cell, is one of *grating*, *flow*, *multi*, *nonselective*. By this classification, the cell in Fig. 2*A* would be classified as a *grating* cell, Fig. 2*B* would be a *flow* cell, and Fig. 2*C* would be a *multi* cell.

Once each cell's type, or preferred stimulus class, has been determined, its preferred spatial frequency can be defined as the one with highest average firing rate among all significant variations of the preferred class (or classes, when cells are labeled *multi*).

We plot the proportion of preferred types at each preferred frequency in Fig. 2*D*; the two separate plots denote units from experimental cohort 1 (0.04–0.24 cpd, $n = 357$ cells, three animals) and cohort 2 (0.04–1.6 cpd, $n = 256$ cells, three animals), respectively. Note the predominance of *gratings* among cells at the lowest frequency, replicating Fig. 1*D*, *Inset*, and the predominance of *flow* and *multi* types at the higher frequencies.

We now examine the distribution of preferred types in two different ways, either including or not including the responses to low-frequency gratings. This is necessary, since the performance measure is a simple spike statistic that is easily dominated by the gratings. First, when low-frequency gratings are included among the stimuli, by the above definitions 45% of the cells respond equally well (i.e., are of the *multi* type), 28% are *flow* cells, 26% prefer *gratings*, and 29% of the cells were not significantly responsive to any of the stimuli displayed (Fig. 2*E*, blue). When low-frequency gratings are not included, so that the comparison is among flows and gratings at the same spatial frequencies, responses favoring *flow* (50%) and *multi* (43%) predominate over those favoring *gratings* (7%) (Fig. 2*E*, red). The difference between these two plots comes from a more detailed analysis: The cells responding strongly to 0.04 cpd can be divided into roughly two subgroups: one that has no significant response other

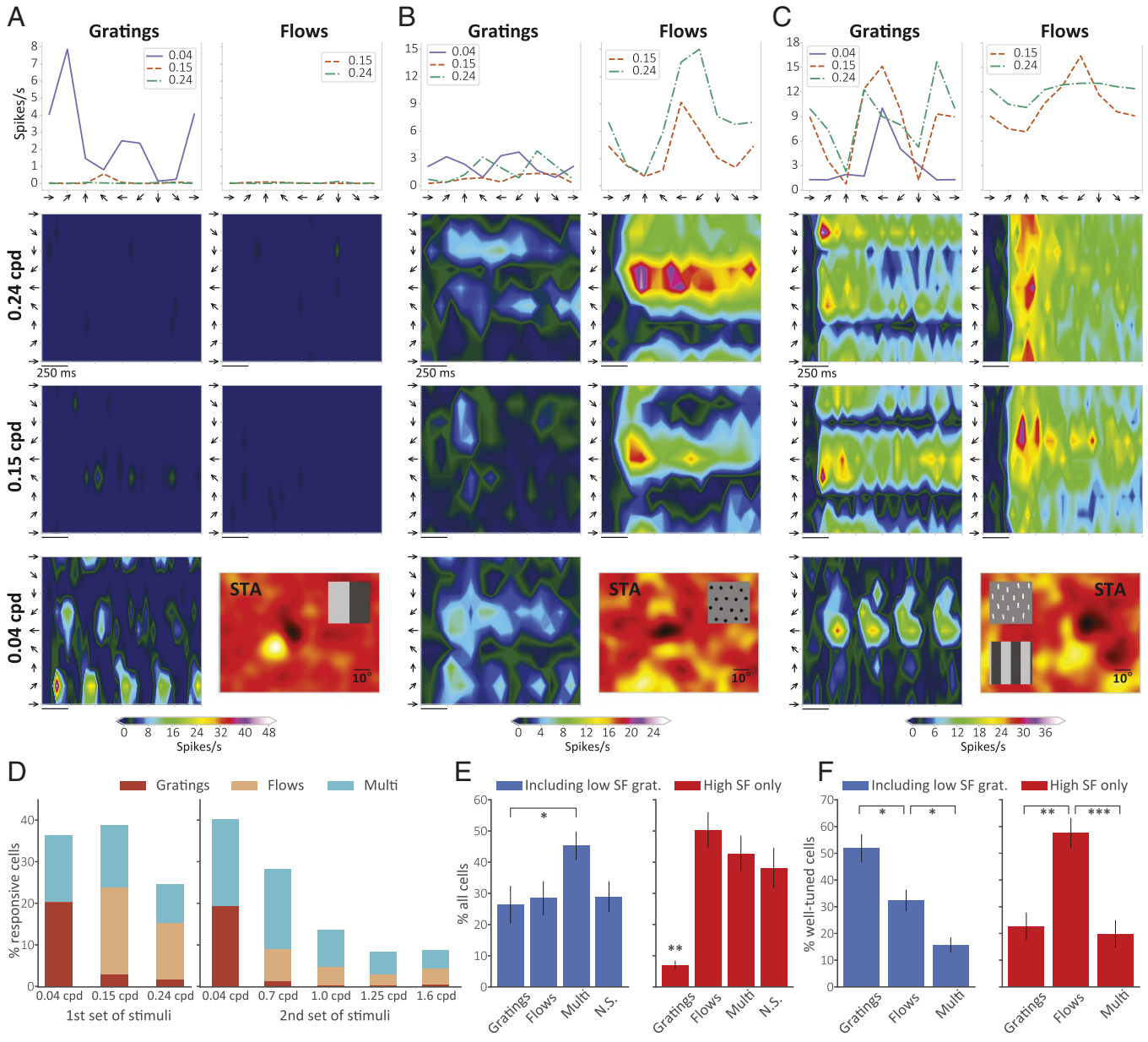

Fig. 2. Variety of responses in V1. (*A–C*) Tuning curves and PSTHs of three example cells in response to drifting gratings and flows at 0.04 cpd, 0.15 cpd, and 0.24 cpd in eight equally spaced directions of motion. Time axis in histograms encompasses an entire period of stimulus presentation (1.5 s). *Insets* in STAs show, at the same scale, stimuli that produced the most significant responses. (*A*) Cell responding to low-frequency gratings only. Bin size is 34 ms. (*B*) Cell responding preferentially to single-dot flows with negative contrast. Bin size is 83 ms. (*C*) Cell responding strongly to both oriented (three dots), positive flows and gratings (at both high and low spatial frequencies). Bin size is 46 ms. (*D*) Distribution of optimal spatial frequency in terms of proportion of cells significantly responding to at least one of the stimuli. In the group of experiments using the first set of stimuli (*D*, *Left*, 0.04–0.24 cpd, $n = 357$ cells, three animals), the majority of cells fired more strongly for stimuli at 0.15 cpd, followed closely by 0.04 cpd. For the second set of stimuli (*D*, *Right*, 0.04–1.6 cpd, $n = 256$ cells, three animals) there was an overwhelming preference for 0.04 cpd, although more than half the cells had optimal spatial frequency in the range 0.7–1.6 cpd. (*E*) Distribution of preferred stimulus among all cells. When low-frequency gratings (0.04 cpd) are included among the stimuli (*E*, *Left*), the majority of cells respond equally well to both classes ("Multi"), followed by only flows and only gratings; 29% of the cells were not significantly responsive ("N.S.") to any of the stimuli displayed ($n = 1,026$ cells; 10 experiments, six animals). When we do not include low-frequency gratings (grat), thereby limiting the comparison with flows and gratings with similar spatial frequencies, there is a significant preference for flows only and for both over gratings only. Comparison of *E*, *Left* and *Right* reveals that ∼20% of cells preferred low-frequency gratings. When we recompute stimulus preference considering only stimuli with comparable spatial frequencies, most cells that preferred low-frequency gratings now either prefer none of the high-frequency stimuli or significantly prefer flows over high-frequency gratings, given that the fraction that prefers both remains essentially constant in the two scenarios. $*P = 0.025$; $**P < 0.001$. Error bars represent SEM. (*F*) Distribution of preferred stimulus among well-tuned cells (i.e., those with OSI > 0.5 or DSI > 0.5), $n = 295$ cells (*Left*) and 241 cells (*Right*); 8 experiments, four animals. Here, note that most of the cells responding to orientation and/or direction will fire more strongly to low-frequency gratings; *F*, *Right* reveals, however, that the fraction of cells well tuned to flows is just as large. And, similarly to *E*, many of the well-tuned cells preferring 0.04 cpd gratings prefer flows to gratings of comparable spatial frequency. $*P < 0.05$; $**P < 0.001$; $***P < 0.0001$. Error bars represent SEM.

than to low-frequency gratings and another that also responds well to flows (or, in fewer cases, to both flows and high-frequency gratings). These plots include all cells. A similar distinction is obtained when only cells well tuned to orientation [orientation selectivity index (OSI) > 0.5] or direction [direction selectivity index (DSI) > 0.5] are considered (Fig. 2*F*).

To summarize, among cells with significant preference for flows or both flows and gratings, responses were distributed across all spatial frequencies explored. For "classical" cells (those that significantly preferred gratings to flows) there is a clear preference for 0.04 cpd with a distribution in accordance with that in ref. 12 (Fig. 1*D*). Curiously, some cells that are well tuned to low-frequency gratings are also well tuned to flows with higher spatial frequency, albeit usually with lower firing rates. Nevertheless, many of these cells have higher firing rates to flows than to gratings of similar spatial frequency, showing that there is some aspect of the flow stimulus that strongly excites these cells despite the fact that the flow elements would not excite the filter predicted by these cells' STAs. In *SI Appendix*, Figs. S1–S13 show plots of responses to the entire stimulus ensemble for these and other cells.

Cells Remain Well Tuned at High Spatial Frequencies. Since higher firing rates do not necessarily imply high orientation or direction selectivity, and since a cell might retain its selectivity at several spatial frequencies (SFs), we investigated the fraction of well-tuned cells (OSI $>$ 0.5 or DSI $>$ 0.5) across spatial frequencies regardless of preferred stimulus (Fig. 3*B*). This is an estimate of the probability of a cell significantly responsive to a certain SF being well tuned.

There are many cells well tuned to direction and/or orientation at all SFs. Cells with high orientation selectivity tend to prefer stimuli in the 0.04- to 0.24-cpd range. The direction-selective cells seem to be more uniformly distributed across SFs, with a preference for intermediate SFs (0.15–0.24 cpd).

Higher Stimulus Selectivity in Superficial and Deep Layers. To further characterize how the response profile of *multi* cells is distributed across stimulus variations, we extend the concept of selectivity indexes such as OSI and DSI (e.g., ref. 12) to compare pairs of stimulus classes. A stimulus selectivity index (SSI) is thus defined for a pair of classes (e.g., flows vs. gratings or one-dot flows vs. three-dot flows) as $(R_{\max} - R_{\min})/(R_{\max})$, where $R_{\max}$ ($R_{\min}$) is the average peak firing rate (FR) of the stimulus with the higher (lower) FR in the pair. Essentially, it measures the difference in FR between two stimuli, relative to the one with highest FR. E.g., an SSI of 0.2 means the FR for the less preferred stimulus is 20% lower than that for the preferred one. When comparing stimulus classes for which there are possibly several stimulus variations in each class, we take the variation that elicited the highest response in each one. Note that the SSI for a cell population assesses how well those cells' responses can be used to differentiate between two stimuli, regardless of which one is the preferred one.

Cells responsive to both flows and high-frequency gratings were found in all cortical layers. Cells in layer 2/3 had significantly higher values of SSI than those in all other layers for differentiating flows from gratings ($P < 10^{-3}$, $P = 10^{-6}$, and $P = 10^{-4}$ for layers 4, 5, and 6, respectively), while cells in layer 5 had significantly lower SSI than those in layers 2/3 ($P < 10^{-4}$) and 6 ($P < 0.05$) when differentiating between flows with opposite contrast polarities and lower than those in layer 2/3 ($P < 0.005$) when differentiating oriented from nonoriented flows (Fig. 4). The same trends were found when only broad-spiking cells (putative excitatory, ref. 12) were considered. Thus, speculatively, cells in the superficial layers could have higher selectivity, while cells in layer 5 could be more invariant to geometry, length, and contrast. This may be related to ref. 12, in which it was reported that layer 5 cells were significantly less linear than cells in other layers.

Preference Among Different Variations of Flow Stimuli Goes Beyond Differences in Spatial Frequency. Among cells that responded significantly to flows, we also compared the average proportion of cells that significantly preferred oriented (three dots) vs. nonoriented flow patterns (single dots) (Fig. 5*A*). Analysis of the entire population across different experiments does not reveal any particular preference, with the vast majority responding to both geometries. However, if analysis is restricted to those cells well tuned to direction and/or orientation, the preference for a specific flow geometry—be it oriented or nonoriented—increases markedly. In particular, there is an overall preference for the oriented patterns.

Fig. 5*B* shows that only a minority of the cells responding to flows prefer negative contrast (15%, on average). The vast majority either prefer positive contrast or respond significantly to both contrast polarities. This difference in preference disappears among cells that are well tuned to direction and/or orientation.

Discussion

Receptive Fields Redux? Cells are routinely classified as "simple" if they exhibit a linear response to moving bars or gratings (27)

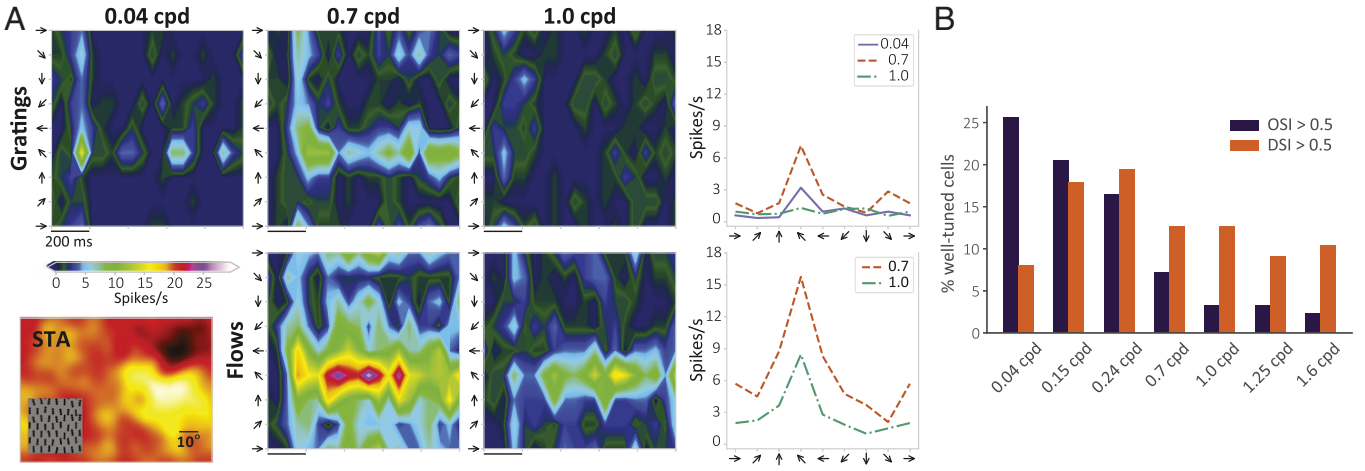

Fig. 3. Cells remain highly selective at higher spatial frequencies. (*A*) Example of cell exhibiting a stronger response to oriented, negative flows at 0.7 cpd and 1.0 cpd compared with gratings at various spatial frequencies. Bin size is 47 ms. (*B*) Overall proportion of well-tuned cells among cells significantly responsive to each spatial frequency (Mann–Whitney *U* test, $P < 0.05$), irrespective of stimulus class. Sample sizes: 0.04 cpd (n = 508), 10 experiments, six animals; 0.15 cpd (n = 385), 0.24 cpd (n = 365), 5 experiments, three animals; and 0.7 cpd (n = 214), 1.0 cpd (n = 214), 1.25 cpd (n = 186), 1.6 cpd (n = 173), 5 experiments, three animals.

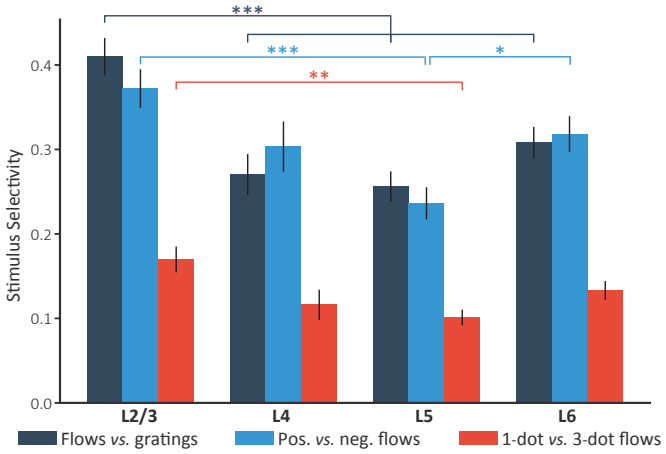

Fig. 4. Cells in different layers have distinct selectivity toward different stimulus classes, as measured by a SSI (main text). ***$P < 0.001$; **$P < 0.005$; *$P < 0.05$. Error bars represent SEM.

and as "complex" if the response is nonlinear (over phase). However, these are operational definitions and depend on the stimuli. Arguments against such classical receptive field concepts are developing (28), and our results contribute to this. Unlike the traditional, optimal feature viewpoint, selectivity does not appear to be 1D; cells can respond linearly to one part of the stimulus ensemble while being nonlinear to others. In particular, we found many cells that exhibit a "linear" response to low-frequency gratings while also responding vigorously at high spatial frequencies to some type of flow (*SI Appendix*, Fig. S16).

The fact that linear methods (e.g., ref. 29) cannot explain such complex and varied responses to an ensemble of stimuli has several implications (*SI Appendix*, Figs. S17 and S18). First, it brings some of the feature variability seen in higher visual areas (e.g., refs. 30 and 31 and references therein) down to V1. Second, since the receptive field is often taken as the signature of functionality, attempts to relate function to structure based on it (e.g., ref. 32) may attribute to "noise" in connectivity genuine features important for neural responses. It follows that stimulus ensembles richer than low-frequency gratings are required to properly assess visual system function. Finally, it suggests that network computations, not individual features, should be the focus of investigation (33).

Flow Responses Suggest Network Computations. At a small scale, responses to high-frequency flow stimuli (i.e., within a receptive field) are reminiscent of the subzones observed in flies (34) and primates (35), each of which can be direction or orientation selective. And, as in flies (36), many cells with a preference for flow stimuli are also contrast selective. At a large scale, our stimuli were displayed wide field, so extraclassical effects may also be playing a role. While investigations of such contextual interactions in mice are just beginning, when stimuli were restricted to gratings (37) and bars (38), only suppressive effects were observed (39). By contrast, in primates the situation is much richer (40–42), and the arrangements of dots and bars in these studies are reminiscent of our flow stimuli. Despite the fact that mice lack orientation columns (43), flow responses are remarkably consistent among the different species. Flow stimuli are also informative about the geometry of surrounding objects (44), although how these geometric, network computations are realized remains an open question.

Materials and Methods

Animal Procedures. Experiments were performed on adult C57/BL6 mice (age 2–6 mo) of either sex. The animals were maintained in the animal facility at the University of California, San Francisco and used in accordance with protocols approved by the University of California, San Francisco Institutional Animal Care and Use Committee. Preparation, extracellular recording, and single-neuron analysis were generally performed as in ref. 45. See *SI Appendix, Materials and Methods* for additional materials and methods.

Design of Flow Stimuli. The flow stimuli consist of local flow elements that move according to an underlying displacement field. The displacement field is defined as a vector in $\mathbb{R}^2$ (i.e., a magnitude and a direction) at each screen position. Each flow element consists of a linear arrangement of n adjacent dots, with $n = 1$ corresponding to a random-dot kinematogram and $n = 2$, 3, 4 corresponding to oriented elements (compare Fig. 1*B*). The stimulus density defines an integer screen lattice. Each flow element is dropped onto this lattice, and then its position is perturbed by a normally distributed random variable. This destroys the impression of a perfectly regular grid of elements.

The displacement field is built on top of this and is organized around a screen partition consisting of a grid of rectangular or hexagonal tiles, with a single displacement vector within each tile. The tiles provide controllable flexibility in the motion. A planar translation results from choosing all displacement vectors the same. To avoid the impression of such simple translations, each displacement vector is "jittered" by sampling from a normal distribution, so that there are now both position jitter and motion jitter. More generally, one can develop more complex motions, either in geometry or in time, by varying the size of the tiles (discreteness) and by varying the displacement directions. For the experiments reported in this paper, a common mean and variance for all vectors in the field were used (see *SI Appendix, Materials and Methods* for specific parameter values).

The movement of each flow element is made even more "lifelike" by controlling its acceleration with a steering force computed as the difference between the element's desired and current directions of motion. This behavior is based on the boids from ref. 46 and on the steering behavior described in ref. 47. Using this, the desired direction can be a function of both the underlying flow field and the proximity between elements; this guarantees that elements do not overlap one another, creating different geometries, densities, or sizes. The final force applied to each element is the resultant between the steering force and a repulsion force exerted by every other element within an allowed distance. The advantage of this approach is that the flow elements can make successive changes in direction as they drift through the flow field by following a smooth and continuous trajectory, without abrupt changes in direction or occlusion. They also wrap around the screen boundaries to preserve a constant number of patterns being shown at all times.

It remains to control the overall luminance and its changes, both for different stages in the trial and for the local dots. For some experiments, the screen luminance during the interstimulus period was set equal to the

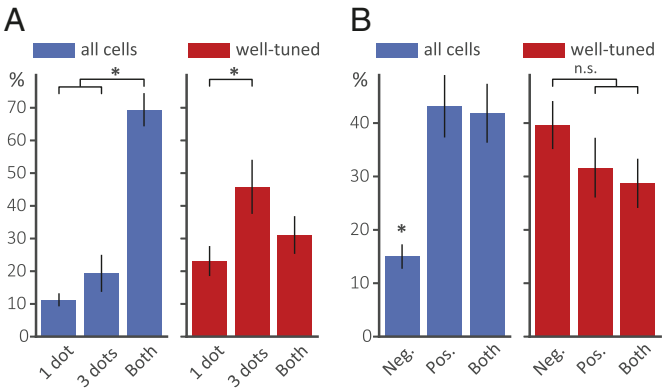

Fig. 5. Preference over flow stimuli variations. Percentages refer to the population of cells that had significant response to at least one flow variation. (*A* and *B*) All cells: $n = 667$, 10 experiments, six animals. Well-tuned cells: $n = 187$, 8 experiments, four animals. Error bars represent SEM (*$P < 0.001$). (*A*) Flow geometry preference. Among all cells responding significantly to flows, most showed no significant prefernce for either type. Among well-tuned cells, oriented flows were preferred over nonoriented flows. (*B*) Flow contrast polarity preference. Among all cells significantly responding to flows, positive polarity was preferred. The population of well-tuned cells showed no overall preference for contrast polarity. n.s., nonsignificant.

global average luminance of the stimulus used in the upcoming trial. This controls for responses that could be caused by the global change in the screen luminance only and not by the actual moving stimuli. However, for this strategy there will still be a change in the luminance of the background when the trial starts. To control for this, i.e., for possible responses due to changes in background luminance, we also ran experiments with a constant gray background both during the flow trials and during the interstimuli intervals. For dot-luminance effects, the diameter of each dot in a multidotted flow element was chosen such that the total area occupied by the element was the same as that of the single-dotted version of the stimulus with the same spatial frequency. In any case, repeated experiments showed that there was little (if any) effect of these different luminance change variations. Code for generating the flow stimuli is available at https://github.com/zuckerlab/FlowStims.

ACKNOWLEDGMENTS. We are grateful to Dr. Sotiris Masmanides of University of California, Los Angeles for supplying the microelectrodes through the NSF NeuroNex program. This work was supported by the Simons Collaboration on the Global Brain, National Eye Institute Grant R01-EY02874, and National Science Foundation Grants CRCNS 1822650 and 1822598. M.P.S. is the recipient of the Research to Prevent Blindness Stein Innovation Award.

1. Fenno L, Yizhar O, Deisseroth K (2011) The development and application of optogenetics. *Annu Rev Neurosci* 34:389–412.
2. Niell CM, Stryker MP (2010) Modulation of visual responses by behavioral state in mouse visual cortex. *Neuron* 65:472–479.
3. Fu Y, et al. (2014) A cortical circuit for gain control by behavioral state. *Cell* 156:1139–1152.
4. Reimer J, et al. (2014) Pupil fluctuations track fast switching of cortical states during quiet wakefulness. *Neuron* 84:355–362.
5. McGinley MJ, et al. (2015) Waking state: Rapid variations modulate neural and behavioral responses. *Neuron* 87:1143–1161.
6. Hess EH, Polt JM (1960) Pupil size as related to interest value of visual stimuli. *Science* 132:349–350.
7. Vinck M, Batista-Brito R, Knoblich U, Cardin JA (2015) Arousal and locomotion make distinct contributions to cortical activity patterns and visual encoding. *Neuron* 86:740–754.
8. Prusky GT, West PW, Douglas RM (2000) Behavioral assessment of visual acuity in mice and rats. *Vision Res* 40:2201–2209.
9. Harris KD, Thiele A (2011) Cortical state and attention. *Nat Rev Neurosci* 12:509–523.
10. Carandini M, Churchland AK (2013) Probing perceptual decisions in rodents. *Nat Neurosci* 16:824–831.
11. Hoy JL, Yavorska I, Wehr M, Niell CM (2016) Vision drives accurate approach behavior during prey capture in laboratory mice. *Curr Biol* 26:3046–3052.
12. Niell CM, Stryker MP (2008) Highly selective receptive fields in mouse visual cortex. *J Neurosci* 28:7520–7536.
13. Juavinett AL, Callaway EM (2015) Pattern and component motion responses in mouse visual cortical areas. *Curr Biol* 25:1759–1764.
14. Palagina G, Meyer JF, Smirnakis SM (2017) Complex visual motion representation in mouse area V1. *J Neurosci* 37:164–183.
15. Douglas R, Neve A, Quittenbaum J, Alam N, Prusky G (2006) Perception of visual motion coherence by rats and mice. *Vision Res* 46:2842–2847.
16. Stirman JN, Townsend LB, Smith SL (2016) A touchscreen based global motion perception task for mice. *Vision Res* 127:74–83.
17. Carandini M, et al. (2005) Do we know what the early visual system does? *J Neurosci* 25:10577–10597.
18. Froudarakis E, et al. (2014) Population code in mouse V1 facilitates readout of natural scenes through increased sparseness. *Nat Neurosci* 17:851–857.
19. Rikhye RV, Sur M (2015) Spatial correlations in natural scenes modulate response reliability in mouse visual cortex. *J Neurosci* 35:14661–14680.
20. Ruderman DL, Bialek W (1994) Statistics of natural images: Scaling in the woods. *Phys Rev Lett* 73:814–817.
21. Simoncelli EP, Olshausen BA (2001) Natural image statistics and neural representation. *Annu Rev Neurosci* 24:1193–1216.
22. Zucker SW (1986) The fox and the forest: Toward a type I/type II constraint for early optical flow.*Proceedings of the ACM SIGGRAPH/SIGART Interdisciplinary Workshop on Motion: Representation and Perception*, eds Badler N, Tsotsos JT (Elsevier North-Holland, Amsterdam), pp 29–62.
23. Abraham R, Marsden JE, Marsden JE (1978) *Foundations of Mechanics* (Benjamin/Cummings Publishing, Reading, MA), Vol 36.
24. Glass L (1969) Moire effect from random dots. *Nature* 223:578–580.
25. Link NK, Zucker SW (1987) Sensitivity to corners in flow patterns. *Spat Vision* 2:233–244.
26. Zucker SW (1985) Early orientation selection: Tangent fields and the dimensionality of their support. *Comp Vision Graphics Image Process* 32:74–103.
27. Hubel DH, Wiesel TN (1959) Receptive fields of single neurones in the cat's striate cortex. *J Physiol* 148:574–591.
28. Fairhall A (2014) The receptive field is dead. Long live the receptive field? *Curr Opin Neurobiol* 25:ix–xii.
29. Schwartz O, Pillow JW, Rust NC, Simoncelli EP (2006) Spike-triggered neural characterization. *J Vis* 6:484–507.
30. Mante V, Sussillo D, Shenoy KV, Newsome WT (2013) Context-dependent computation by recurrent dynamics in prefrontal cortex. *Nature* 503:78–84.
31. Eichenbaum H (2017) Barlow versus Hebb: When is it time to abandon the notion of feature detectors and adopt the cell assembly as the unit of cognition? *Neurosci Lett* 680:88–93.
32. Iacaruso MF, Gasler IT, Hofer SB (2017) Synaptic organization of visual space in primary visual cortex. *Nature* 547:449–452.
33. Yuste R (2015) From the neuron doctrine to neural networks. *Nat Rev Neurosci* 16:487–497.
34. Krapp HG, Hengstenberg B, Hengstenberg R (1998) Dendritic structure and receptive-field organization of optic flow processing interneurons in the fly. *J Neurophysiol* 79:1902–1917.
35. Anzai A, Peng X, Van Essen DC (2007) Neurons in monkey visual area v2 encode combinations of orientations. *Nat Neurosci* 10:1313–1321.
36. Clark DA, et al. (2014) Flies and humans share a motion estimation strategy that exploits natural scene statistics. *Nat Neurosci* 17:296–303.
37. Self MW, et al. (2014) Orientation-tuned surround suppression in mouse visual cortex. *J Neurosci* 34:9290–9304.
38. Samonds JM, Feese BD, Lee TS, Kuhlman SJ (2017) Nonuniform surround suppression of visual responses in mouse V1. *J Neurophysiol* 118:3282–3292.
39. Adesnik H, Bruns W, Taniguchi H, Huang ZJ, Scanziani M (2012) A neural circuit for spatial summation in visual cortex. *Nature* 490:226–231.
40. Allman J, Miezin F, McGuinness E (1985) Stimulus specific responses from beyond the classical receptive field: Neurophysiological mechanisms for local-global comparisons in visual neurons. *Annu Rev Neurosci* 8:407–430.
41. Knierim JJ, Van Essen DC (1992) Neuronal responses to static texture patterns in area V1 of the alert macaque monkey. *J Neurophysiol* 67:961–980.
42. Zipser K, Lamme VA, Schiller PH (1996) Contextual modulation in primary visual cortex. *J Neurosci* 16:7376–7389.
43. Ohki K, Reid RC (2007) Specificity and randomness in the visual cortex. *Curr Opin Neurobiol* 17:401–407.
44. Ben-Shahar O, Zucker SW (2004) Geometrical computations explain projection patterns of long-range horizontal connections in visual cortex. *Neural Comput* 16:445–476.
45. Dadarlat MC, Stryker MP (2017) Locomotion enhances neural encoding of visual stimuli in mouse V1. *J Neurosci* 37:3764–3775.
46. Reynolds CW (1987) Flocks, herds and schools: A distributed behavioral model. *ACM Computer Graphics* 21:25–34.
47. Reynolds CW (1999) Steering behaviors for autonomous characters. *Proceedings of the 1999 Game Developers Conference* (Miller-Freeman, San Francisco), pp 763–782.

PNAS
www.pnas.org

Supplementary Information for

Flow stimuli reveal ecologically-appropriate responses in mouse visual cortex

Luciano Dyballa, Mahmood S. Hoseini, Maria C. Dadarlat, Steven W. Zucker, Michael P. Stryker

Michael P. Stryker.
E-mail: stryker@phy.ucsf.edu

This PDF file includes:

Supporting Information Text

Materials and methods

Animal procedures. Experiments were performed on adult C57BL/6J mice (age 2–6 months) of either sex. All protocols and procedures are approved by the University of California–San Francisco Institutional Animal Care and Use Committee. Animals were maintained on a 12 h light/12 h dark cycle. Recordings were performed during the dark cycle, more active phase of the cycle.

Preparation of mice for extracellular recording on the spherical treadmill. Recordings were done on alert mice free to run on a spherical treadmill modified from the design described by (2). Briefly, a polystyrene ball (200 mm diameter, Graham Sweet Studios) is placed on a shallow polystyrene bowl (250 mm in diameter, 25 mm thick) with a single air inlet at the bottom. Two optical USB mice, placed 1 mm away from the edge of the ball, are used to sense rotation of the floating ball and transmit signals to the data analysis system using custom driver software. The optical mice acquire locomotion information in an event-driven mode at up to 300 Hz. The data is then translated to the net physical displacement of the top surface of the ball.

During recordings, the animal's head is fixed to a rigid crossbar above the floating ball by screwing a titanium headplate that is attached to animal's skull. The headplate—consisting of two side bars and a circular center with a 5 mm central opening—is cemented to the skull one week before recording using surgical procedures as described by (2). Briefly, animals are anesthetized with isofluorane in oxygen (3% induction, 1.5% maintenance), given subcutaneous Meloxicam (10 mg/kg) as a postoperative analgesic and a subcutaneous injection of 0.2 mL of saline to prevent postoperative dehydration. After a scalp incision, the fascia is cleared from the surface of the skull and the metal headplate is then attached with Metabond (Parkell Co.), covering the entire skull, except for the region in the center of the headplate, which is covered with a 0.2% benzethonium chloride solution (New-Skin Liquid Bandage) to protect the skull. The animal is then allowed to recover on a heating pad. Several days following headplate implant, the animal is allowed to habituate to the recording setup and learn to control the ball by spending time on the floating ball over the course of 2–3 days (15 min to 1 h). The average amount of time the animal spent running (threshold used 0.5 cm/s) was 23% $\pm$ 3% (s.e.m.) of the total experiment. Excluding the running trials did not result in any statistically significant change in the results.

Visual stimuli. Visual stimuli were presented with gamma-correction correction on a monitor (Nanao Flexscan, 30 $\times$ 40 cm, 60 Hz refresh rate, 32 cd/m^2 mean luminance) placed 25 cm from the mouse, subtending 60°–75° of visual space. For current source density (CSD) analysis, we present a contrast-reversing square checkerboard (0.04 cpd, square-wave reversing at 1 Hz). For localization of receptive fields by spike-triggered averaging we presented spatiotemporal band-limited noise patterns, as in (1).

To characterize neural responses with single-unit recordings, we presented interleaved drifting square-wave grating stimuli and flow stimuli (shown at 60 frames/s) moving in 8 directions at a temporal frequency of 4 cycle/s over two sets of spatial frequencies: the first included 0.04, 0.15, and 0.24 cpd (100% contrast, trial duration 1.5 s); the second included 0.04, 0.7, 1.0, 1.25, and 1.6 cpd (50% contrast, trial duration 1.0 s). Only gratings were shown at 0.04 cpd. We used flow stimuli with two different geometries. The first are non-oriented single-dot flows, and the other are oriented flow elements with 3 or 4 dots. Both oriented and non-oriented variations had one version with positive contrast (white dots against a black or gray background), and another with negative contrast (black dots against a white or gray background). Dominant spatial frequency contents of 0.15 cpd, 0.24 cpd, 0.7 cpd, 1.0 cpd, 1.25 cpd, and 1.6 cpd were used, corresponding to the following dot diameters, in degrees of visual angle (resp., spacing between dot centers, in multiples of dot diameter): 2.1 (3), 1.5 (3), 0.7 (2), 0.5 (2), 0.4 (2), 0.3 (2) for single dots; for n dots, the diameter is divided by $\sqrt{n}$ so as to preserve the total area occupied by flow elements. For all flow stimuli, both parallel and jittered versions (0 and 0.1 rad std. dev. of flow field direction distribution, respectively) were used, with no detectable difference in the results; flow field tile side: 2.5 times the space between dots; initial positions on the lattice had std. dev. equal to 10% of dot spacing. All stimuli variations were repeated 20–25 times according to a randomized sequence. Contrast and trial duration were the same for all stimuli used in the same experiment.

Extracellular recording in awake mice. Extracellular microelectrode recording procedure was slightly modified from (2). On the day of recording, the animal is again anesthetized as described above. The liquid bandage is removed, and the skull is thinned and removed to produce a craniotomy 1–2 mm in diameter centered above the monocular zone of V1 (2.5–3 mm lateral to midline, 1–2 mm anterior to lambda). This small opening is enough to allow insertion of a 1.1-mm-long double-shank 128-channel probe (3), fabricated by the Masmanidis laboratory (University of California–Los Angeles) and assembled by the Litke laboratory (University of California–Santa Cruz). The electrode is placed at an angle of 30°–45° to the cortical surface and inserted to a depth of 500–1000 μm below the cortical surface. A period of 30 min to 1 h is allowed to pass before recording begins. For each animal, the electrode is inserted no more than twice. Microelectrode and stimulus synchronization data are acquired using an Intan Technologies RHD2000Series Amplifier Evaluation System, sampled at 25 kHz.

Single-neuron analysis. Single units are identified using MountainSort (4), which runs in approximately 2$\times$ real time for fully automated spike sorting of data from our 128-site electrodes. Manual curation after a run on one hour of data takes an additional half hour, typically yielding 150 isolated single units.

Cortical layer. The cortical layer containing each isolated unit is determined using current source-density (CSD) analysis on data collected during presentations of contrast-reversing square checkerboard. Briefly, extracellular voltages sampled at 20 kHz are bandpass filtered between 1 and 300 Hz to obtain local field potentials (LFPs) and then averaged across all 1 s positive-phase presentations of the checkerboard. Second spatial derivative of the average LFP traces along the length of the silicon probe provides us with the profile of CSD. The borders between layers 2/3–4, 4–5, and 5–6 are identified by spatiotemporal patterns of sinks and sources in the CSD plot ((5); for example see Fig. 1C of (6)).

Data analysis. Isolated single units that stopped firing altogether after a certain time of the recording or that only started firing after some time were assumed to have moved away or toward the multielectrode array, respectively; therefore the trials with zero spikes at the beginning and end of recordings were discarded.

An orientation selectivity index (OSI) was defined as: $(R_{\mathrm{pref}}-R_{\mathrm{ortho}})/(R_{\mathrm{pref}}+R_{\mathrm{ortho}})$, where $R_{\mathrm{pref}} = (R_{\mathrm{peak\_dir}}+R_{\mathrm{peak\_dir}+\pi})$ is the response (average firing rate) for the preferred orientation and $R_{\mathrm{ortho}} = (R_{\mathrm{ortho\_dir}} + R_{\mathrm{ortho\_dir}+\pi})$ is the response for the orientation orthogonal to the preferred one. A direction selectivity index (DSI) was defined as: $(R_{\mathrm{pref}} - R_{\mathrm{null}})/(R_{\mathrm{pref}} + R_{\mathrm{null}})$, where R_{pref} is the response (average firing rate) for the preferred orientation and R_{null} is the response for the null orientation (π rad apart from the preferred one). A stimulus selectivity index (SSI) was defined for a pair of stimuli as $(R_{\mathrm{max}} - R_{\mathrm{min}})/(R_{\mathrm{max}})$, where R_{max} (R_{min}) is the average peak firing rate of the stimulus with higher (lower) firing rate in the pair.

PSTHs were plotted using a Gaussian interpolation kernel. Bin sizes were chosen following (7). STAs were also plottted using a Gaussian kernel.

Linearity of response was computed by first computing spike histograms with 50 ms bins and subtracting the spontaneous rate. A discrete Fourier transform was then applied and the F1/F0 calculated as the ratio between the first harmonic (F1) and the mean firing rate (F0). To account for the inherent stochasticity of the flow stimuli (which introduces a random phase at each trial), the linearity of response were computed as the mean of the F1/F0 values obtained for each individual trial.

Power spectra of the stimuli were computed with a fast Fourier transform algorithm. Due to the stochasticity of the flow stimuli, the spectra are averages over 40 instances. Data were not treated with any window.

Supplementary Movie 1. Examples of flow stimuli from cohort 1 (see text, 0.15 and 0.24 cpd, positive and negative contrast, 1-dot and 3-dot stimuli).

Supplementary Movie 2. Examples of flow stimuli from cohort 2 (see text, 0.7, 1.0, 1.25, and 1.6 cpd, positive and negative contrast, 1-dot and 3-dot stimuli).

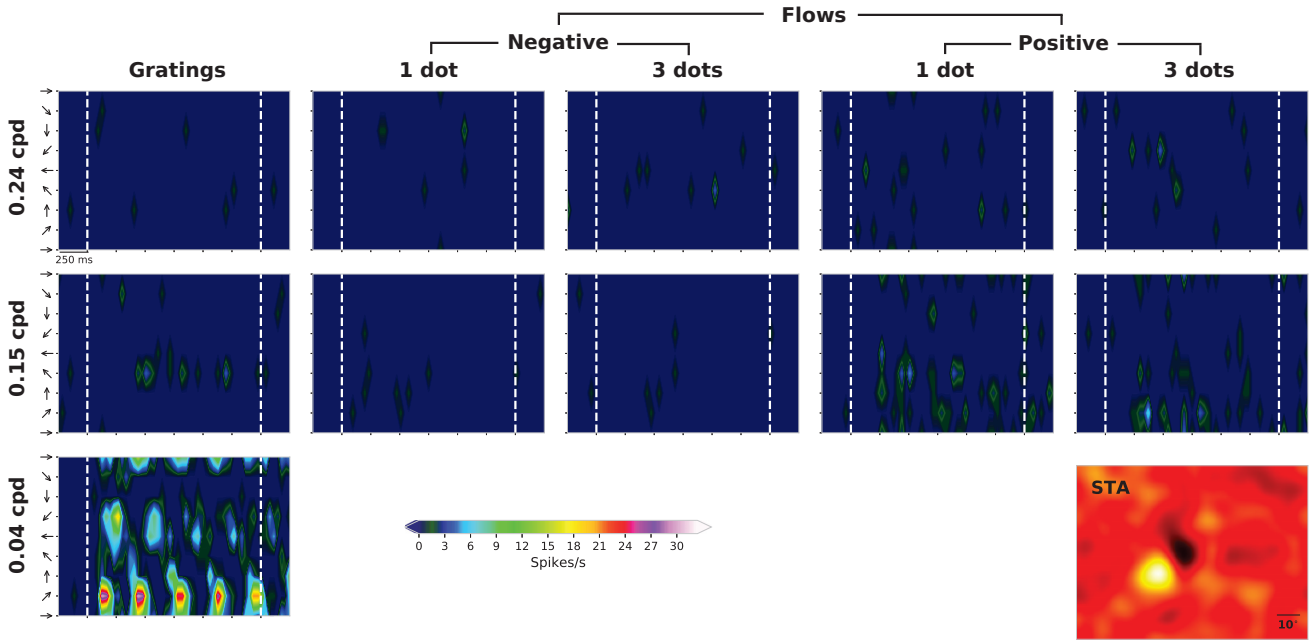

Fig. S1. Full response profile for cell in Fig. 2A in the main text. Bin size 34 ms; vertical dashed lines indicate stimulus onset and offset. Spike-triggered average (STA) latency 99 ms.

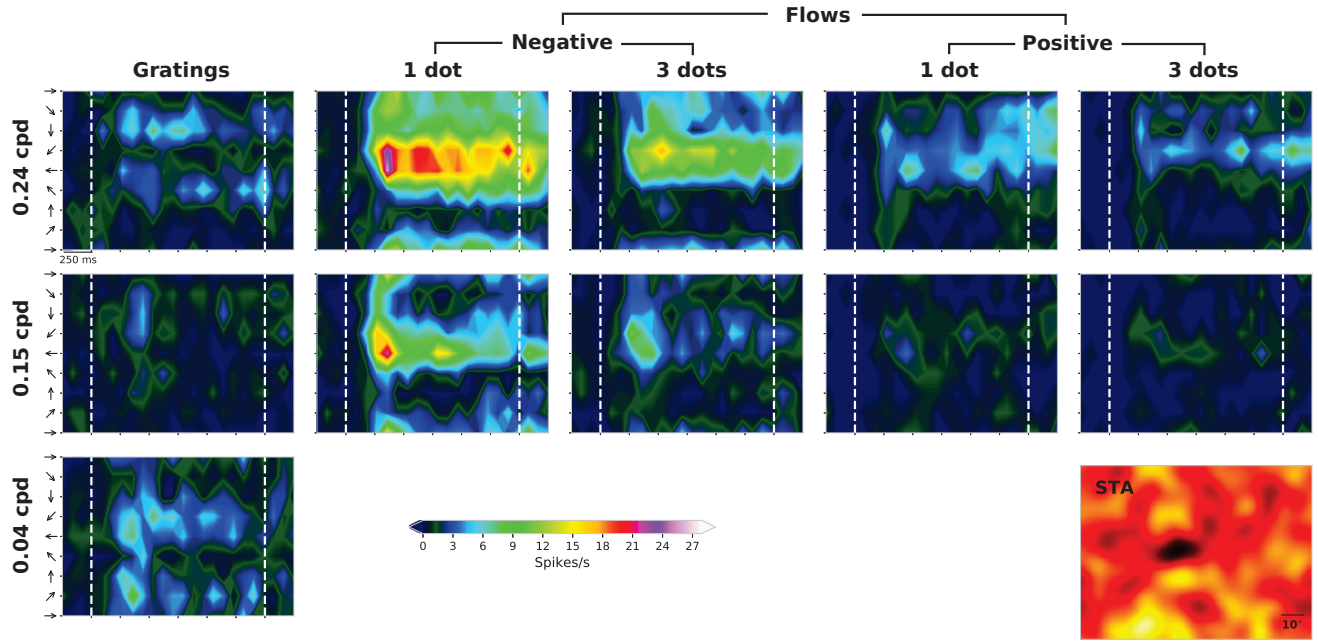

Fig. S2. Full response profile for cell in Fig. 2B in the main text. Bin size 83 ms; vertical dashed lines indicate stimulus onset and offset. Spike-triggered average (STA) latency 99 ms.

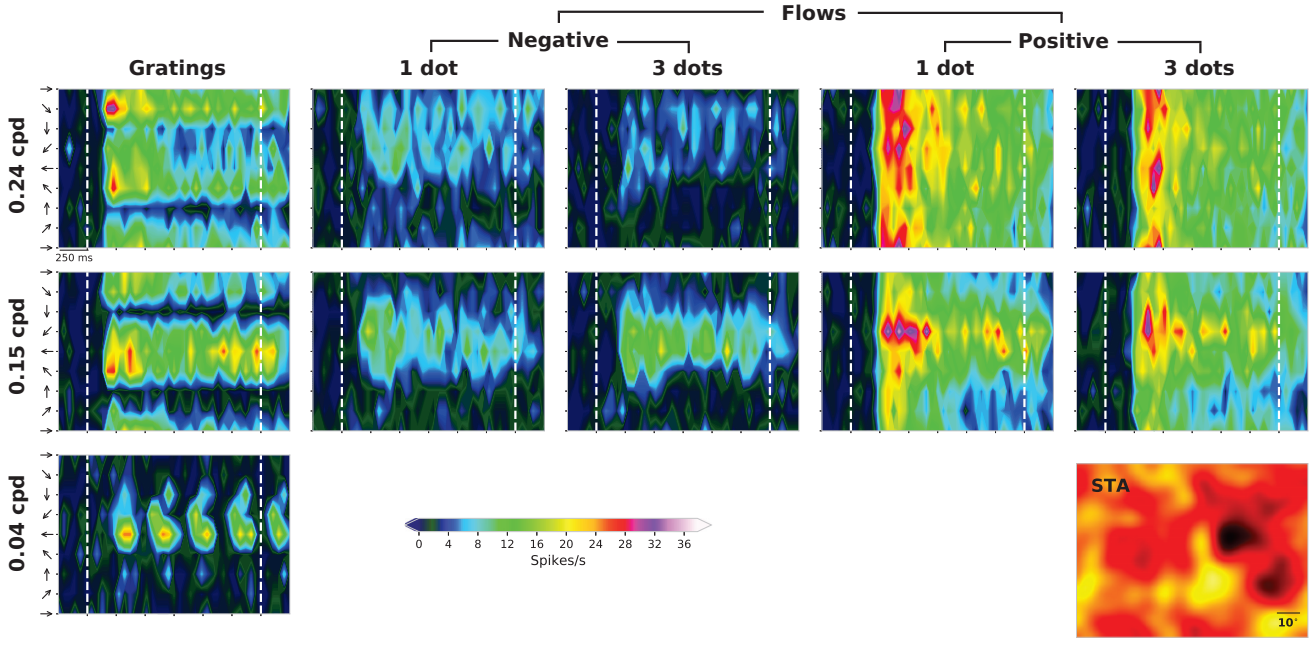

Fig. S3. Full response profile for cell in Fig. 2C in the main text. Bin size 46 ms; vertical dashed lines indicate stimulus onset and offset. Spike-triggered average (STA) latency 66 ms.

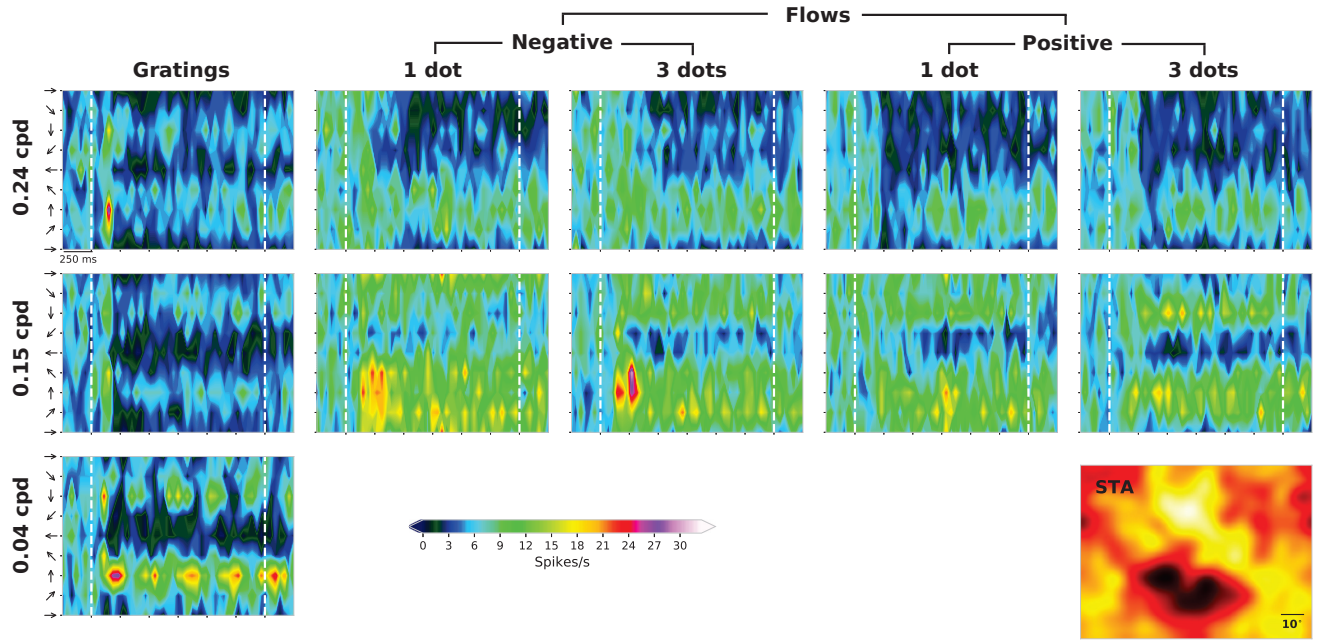

Fig. S4. Cell responding to all stimuli, despite its linear-like response to low-frequency gratings. Bin size 39 ms; vertical dashed lines indicate stimulus onset and offset. Spike-triggered average (STA) latency 99 ms.

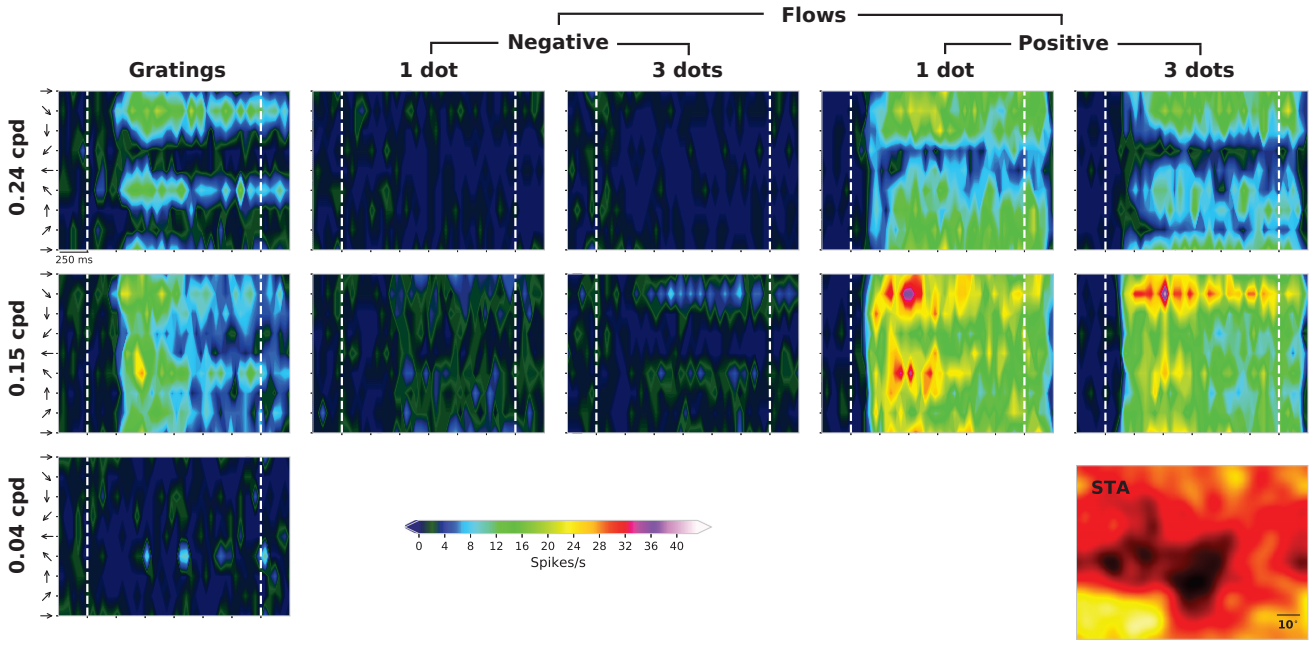

Fig. S5. Cell responding to high frequency gratings and positive flows. Bin size 42 ms; vertical dashed lines indicate stimulus onset and offset. Spike-triggered average (STA) latency 99 ms.

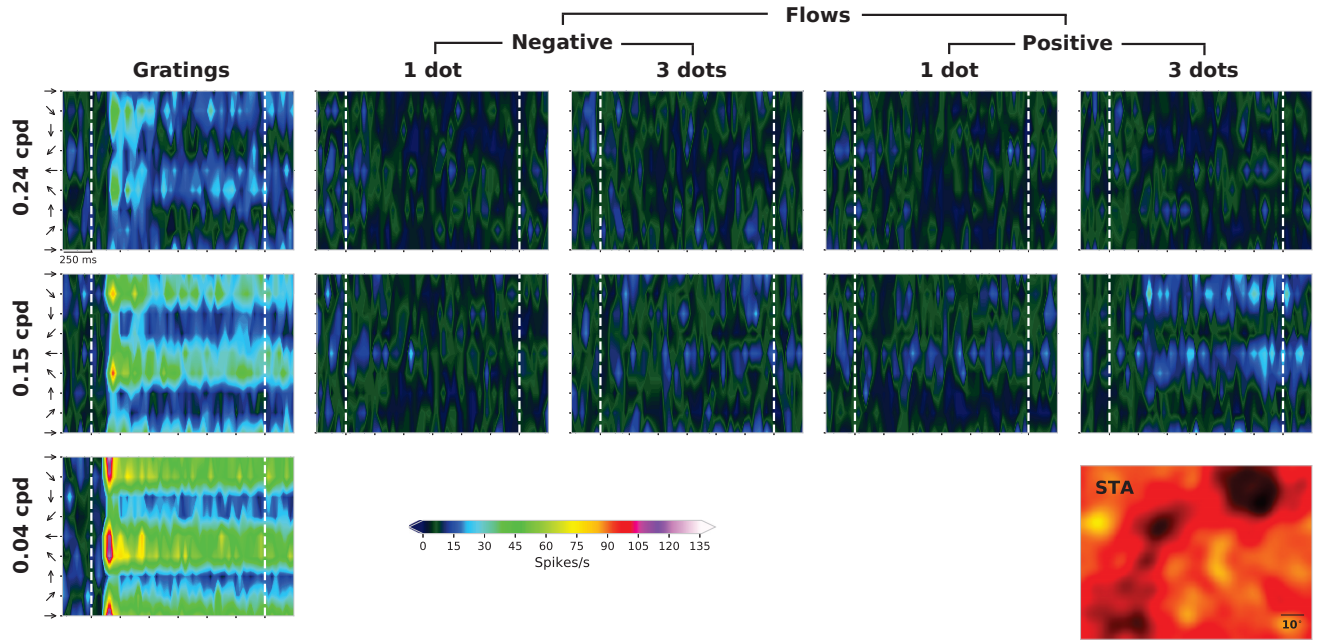

Fig. S6. Cell responding to gratings at multiple spatial frequencies. Bin size 31 ms; vertical dashed lines indicate stimulus onset and offset. Spike-triggered average (STA) latency 66 ms.

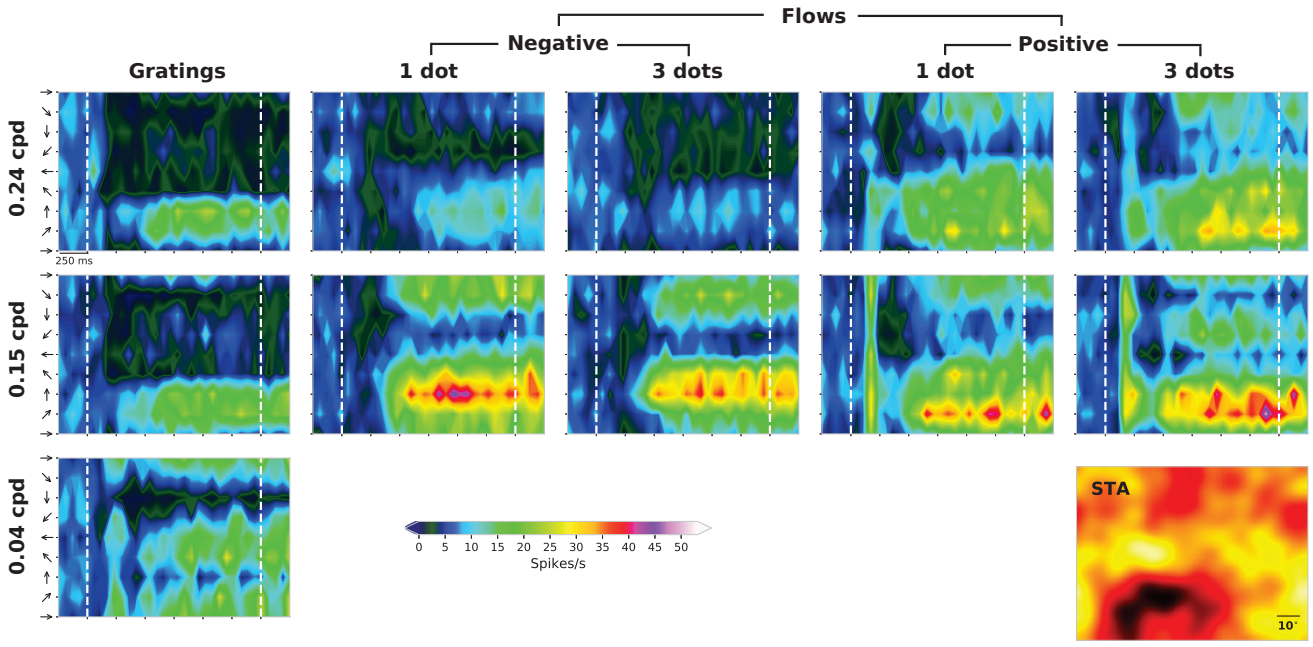

Fig. S7. Cell responding to all stimuli, some with directional tuning, others with orientational tuning; the preferred direction of motion also varies depending on the stimulus. Response to low frequency gratings is linear-like, as suggested by its STA. Bin size 58 ms; vertical dashed lines indicate stimulus onset and offset. Spike-triggered average (STA) latency 165 ms.

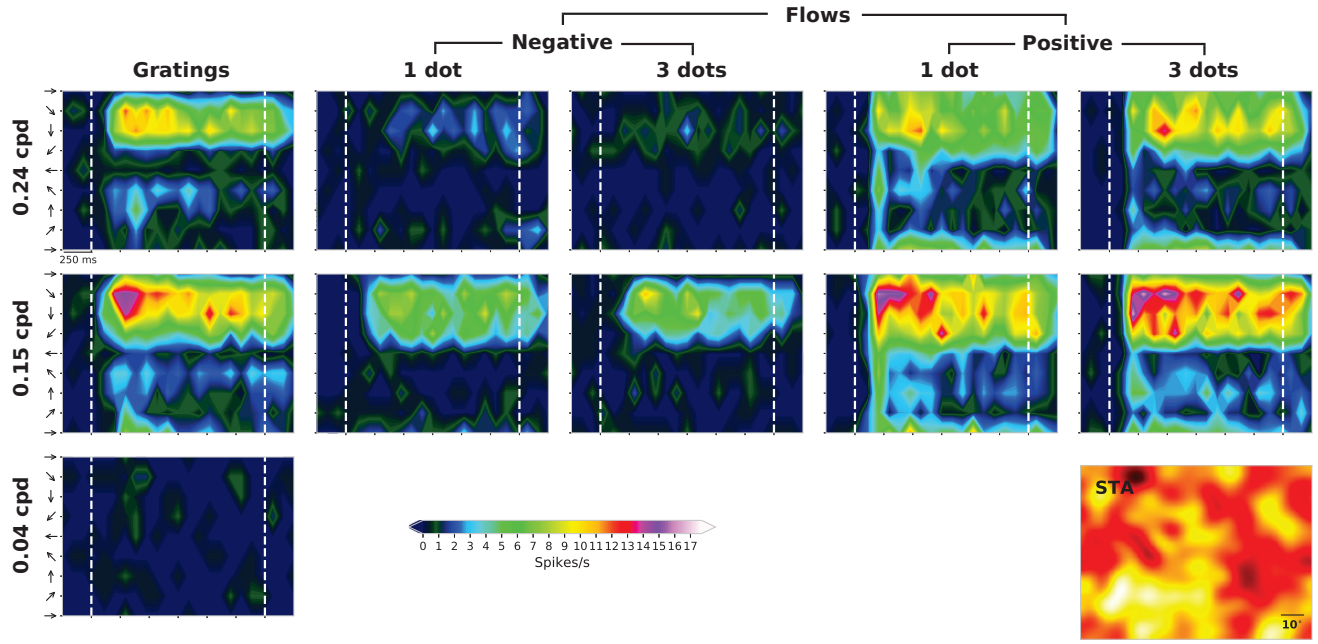

Fig. S8. Cell tuned to direction, consistent across stimuli. Negative and positive flows have distinct spatial frequency tuning. Bin size 86 ms; vertical dashed lines indicate stimulus onset and offset. Spike-triggered average (STA) latency 66 ms.

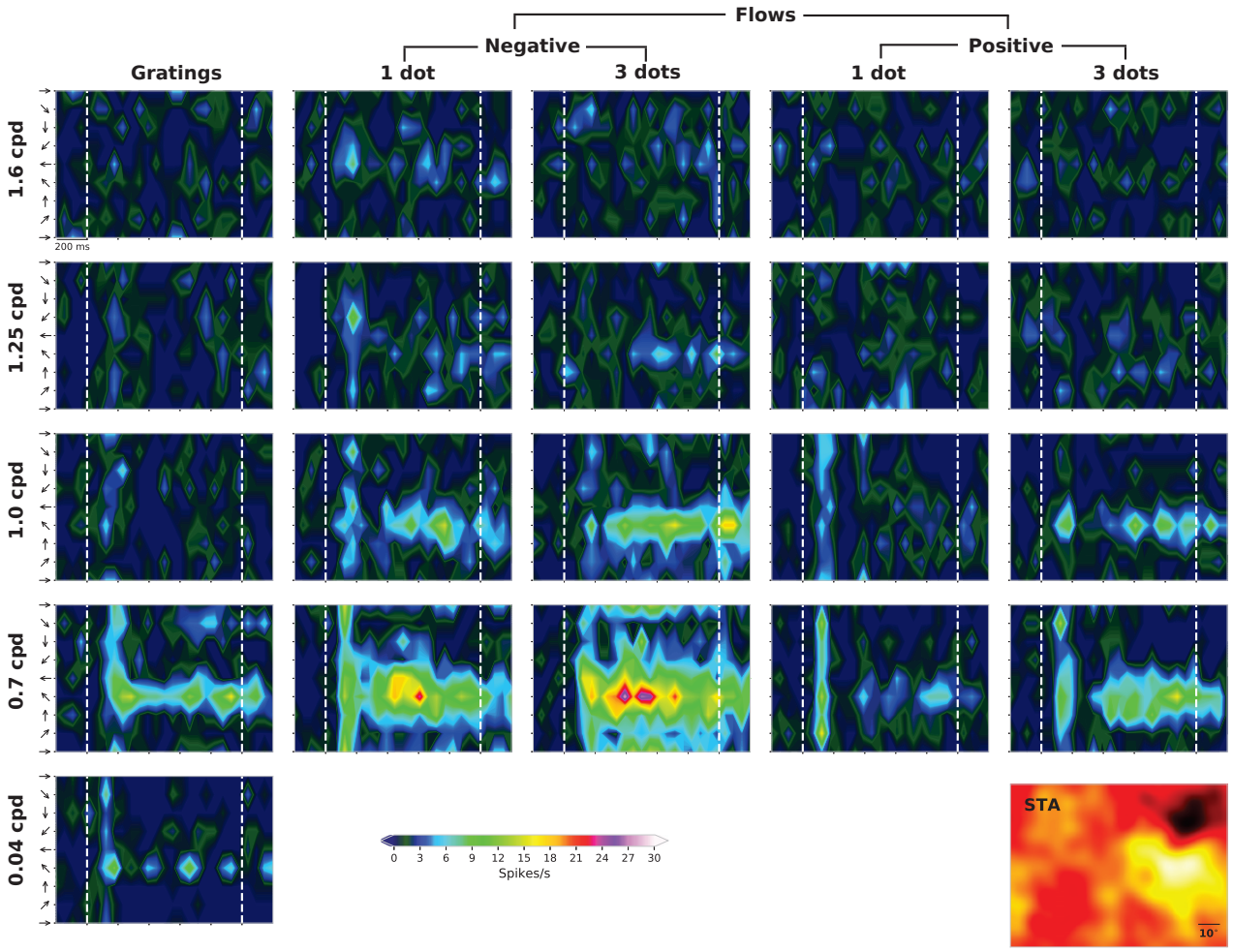

Fig. S9. Full response profile for cell in Fig. 3A in the main text. Bin size 51 ms; vertical dashed lines indicate stimulus onset and offset. Spike-triggered average (STA) latency 99 ms.

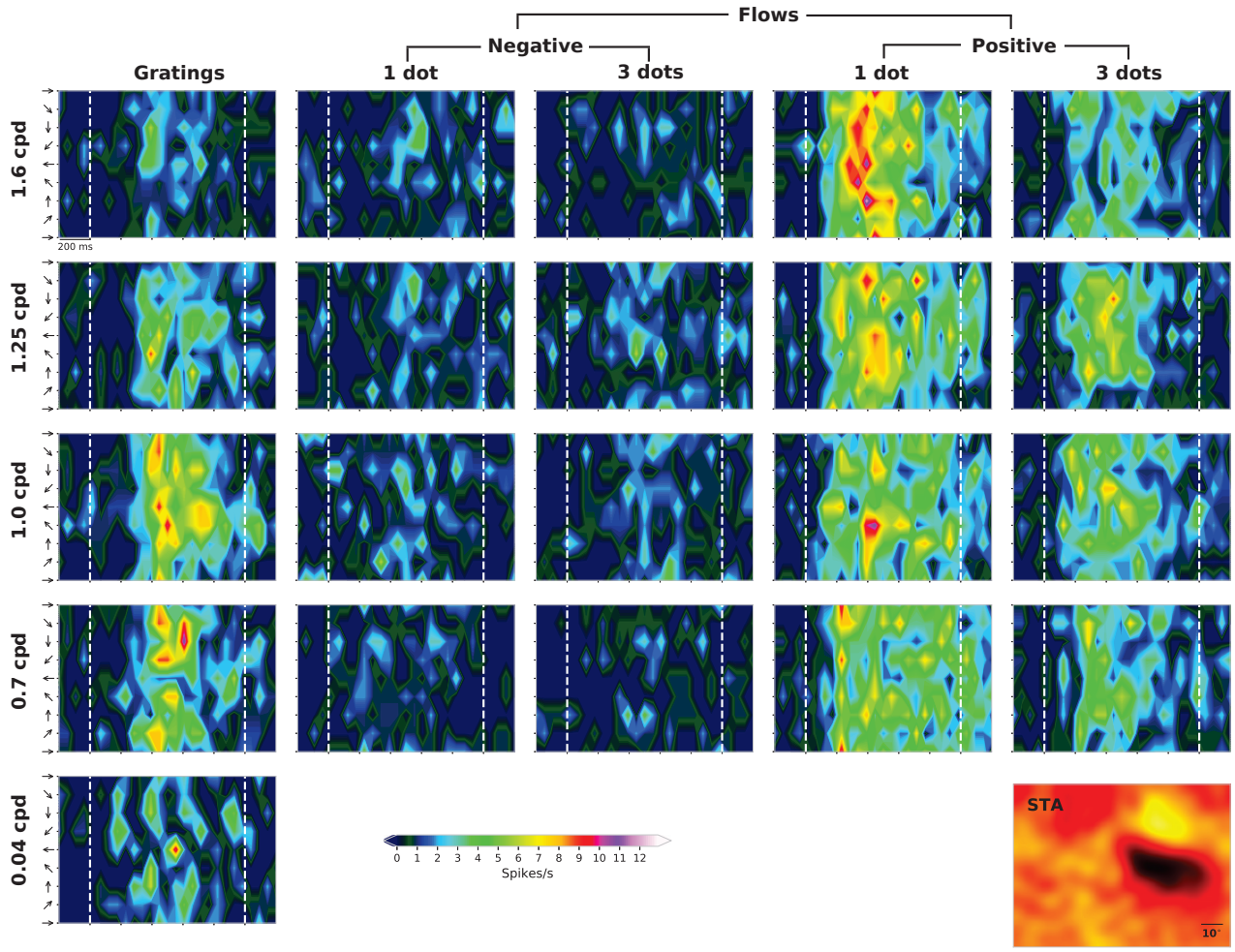

Fig. S10. Cell with peak response to positive 1-dot flows at 1.6 cpd. Interestingly, despite its linear-like response to gratings at 0.04 cpd and clear STA, its response to both gratings and flows at higher frequencies is not well-tuned. Bin size 51 ms; vertical dashed lines indicate stimulus onset and offset. Spike-triggered average (STA) latency 66 ms.

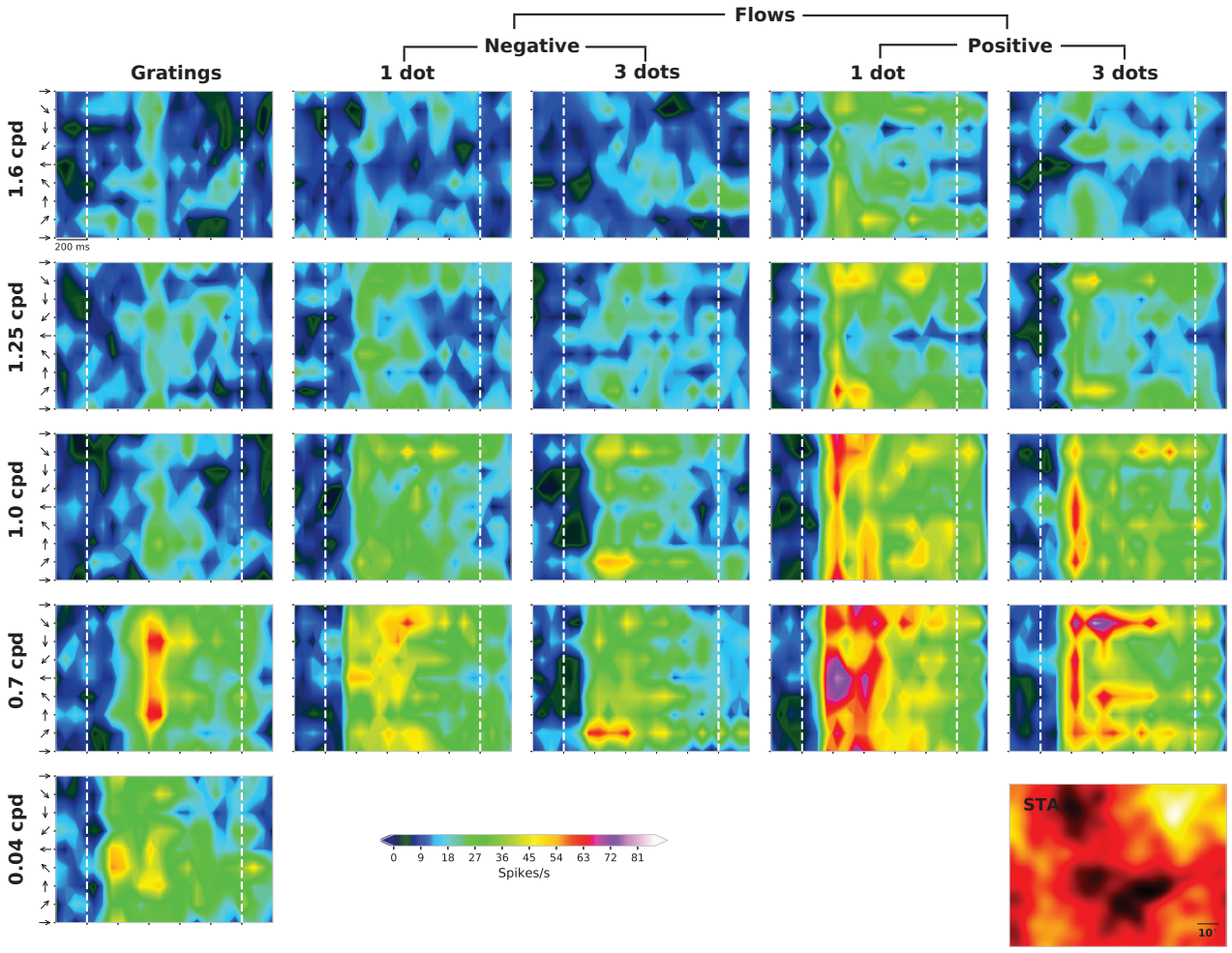

Fig. S11. Cell responding to multiple directions at various spatial frequencies. Bin size 59 ms; vertical dashed lines indicate stimulus onset and offset. Spike-triggered average (STA) latency 132 ms.

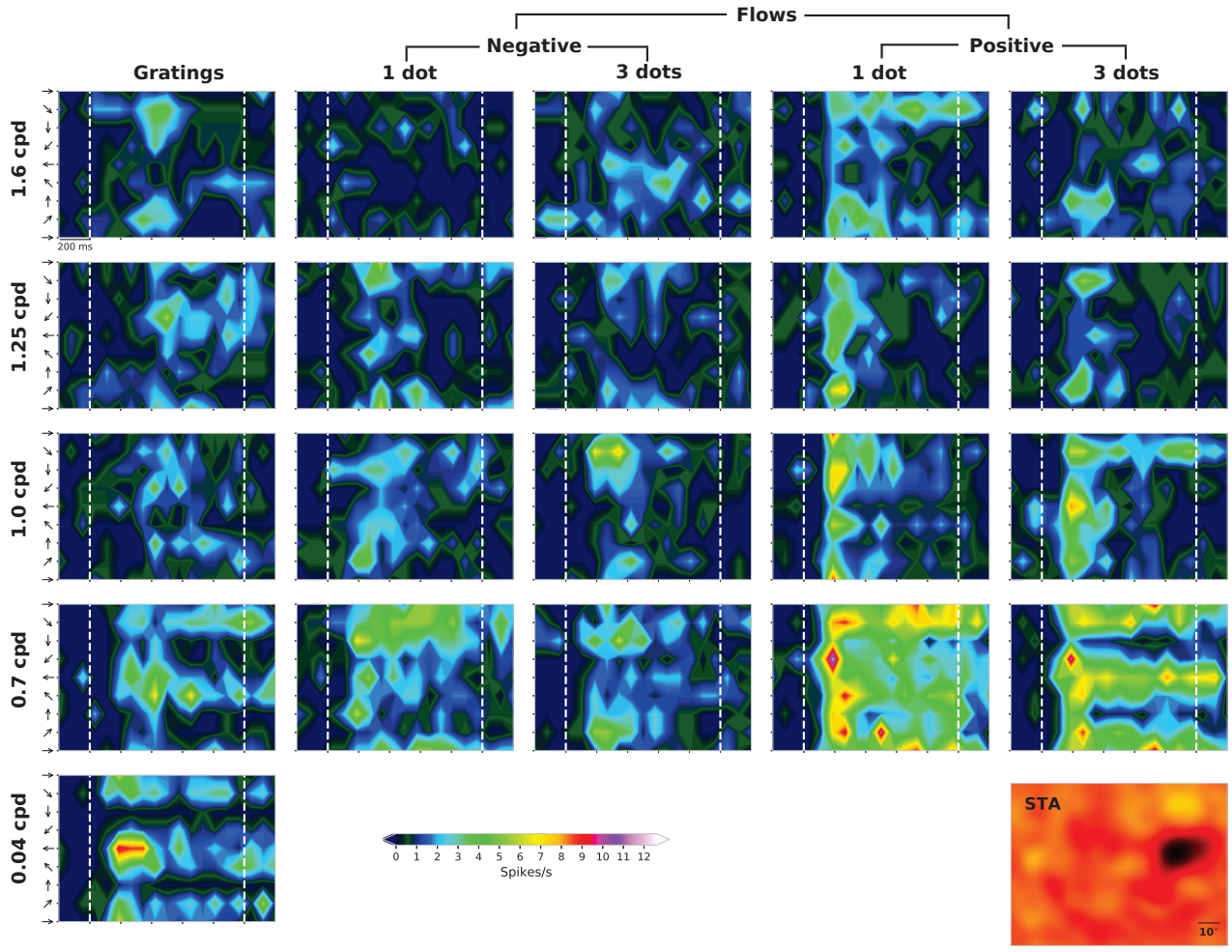

Fig. S12. Cell preserves the same orientation tuning at 0.04-0.7 cpd (gratings) and 0.7-1.0 cpd (positive flows). The oriented flows (3 dots) are more well-tuned than the single-dot flows. Bin size 74 ms; vertical dashed lines indicate stimulus onset and offset. Spike-triggered average (STA) latency 132 ms.

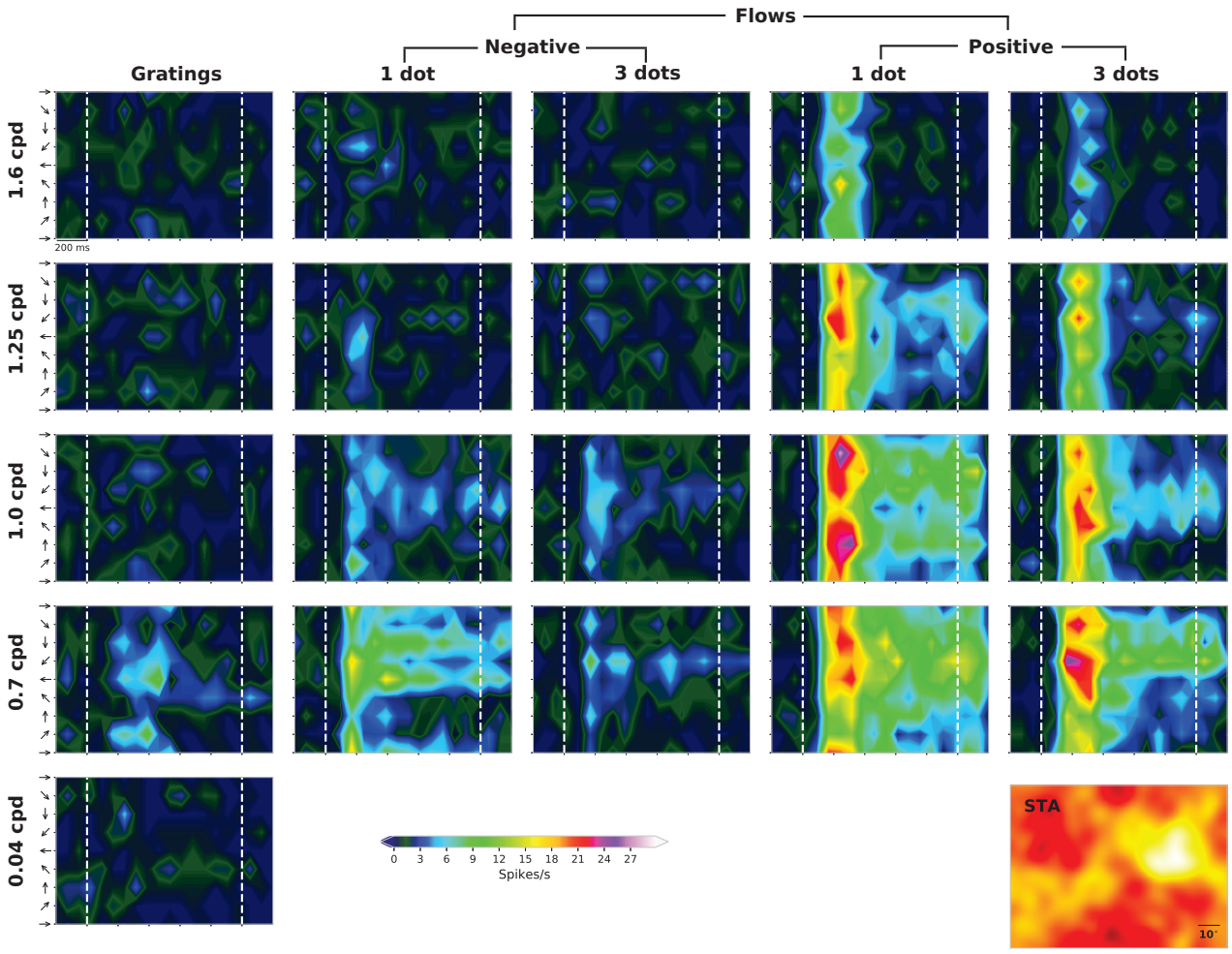

Fig. S13. Cell responding almost exclusively to high frequency flows. Interestingly, direction preferences seem to change between positive 1- and 3-dot flows (especially at 1.0 cpd), as well as between different spatial frequencies (e.g., the two-peaked tuning curve seen for positive 1-dot flows at 1.0 cpd becomes four-peaked at 1.6 cpd). Bin size 70 ms; vertical dashed lines indicate stimulus onset and offset. Spike-triggered average (STA) latency 99 ms.

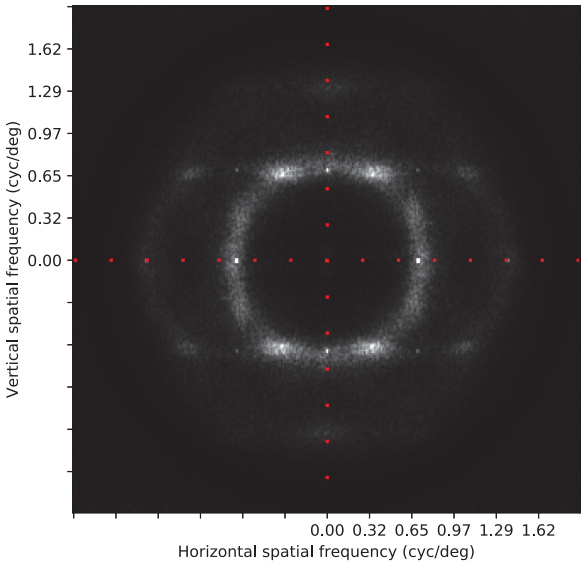

Fig. S14. Example of 2-D frequency spectrum of a 1-dot flow with peak at 0.7 cpd, averaged over 15 frames taken from different trials.

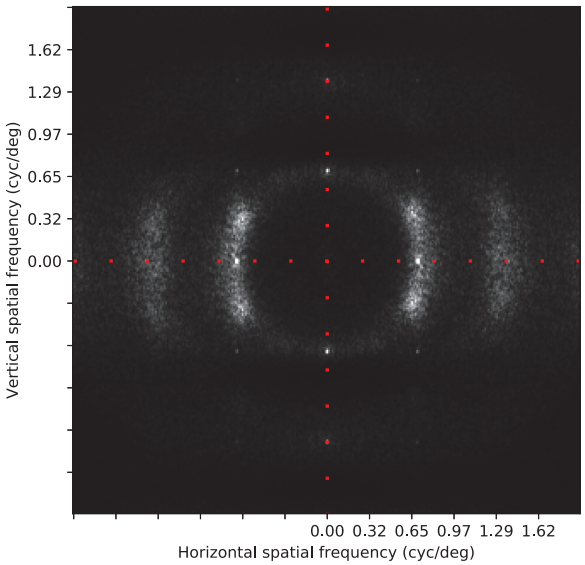

Fig. S15. Example of 2-D frequency spectrum of a 3-dot flow with peak at 0.7 cpd, averaged over 15 frames taken from different trials.

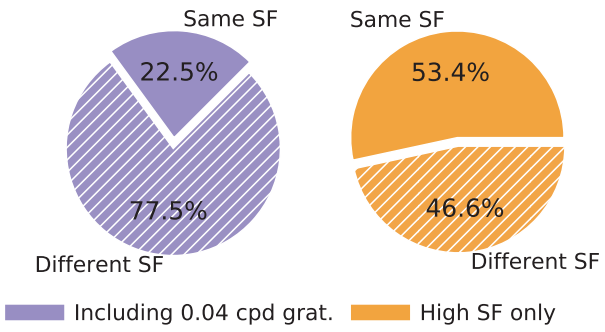

Fig. S16. Comparison of spatial frequency (SF) preference across stimulus class (flows *vs.* gratings) for MULTI cells. Note that, since there are no flows at 0.04 cpd, any MULTI cell whose preferred grating stimulus is at that frequency will necessarily have a different SF for its preferred flow stimulus. Furthermore, given the overwhelming preference for gratings at 0.04 cpd (as seen in Fig. 2), the result from the left chart is somewhat expected. Therefore, it is also informative to look at how likely it is for the SF preference to be preserved across flows and gratings when considering higher spatial frequencies only. The chart on the right shows that, in that case, tuning preference is preserved for the majority of cells.

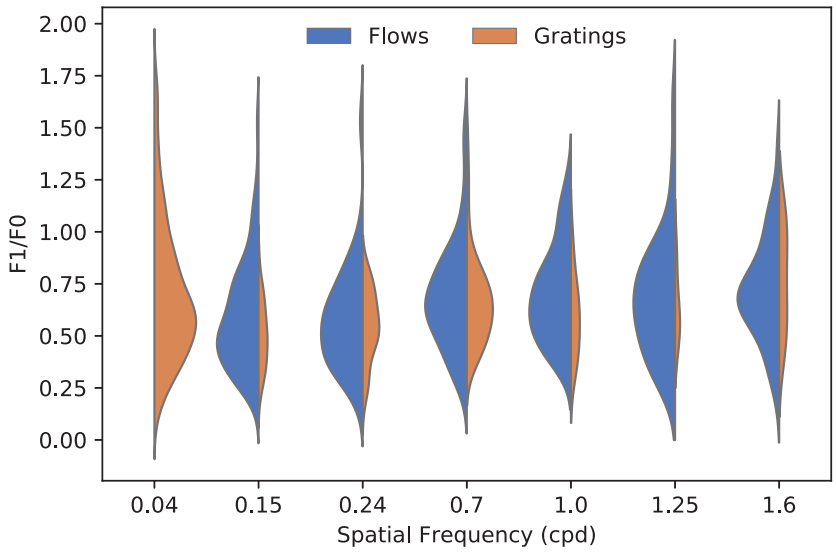

Fig. S17. Distribution of linearity of response to preferred flow and/or grating stimuli. Total area at each spatial frequency (sum of the distributions for flows and gratings) is normalized to 1. For MULTI cells, the F1/F0 values for both their preferred flow and grating stimuli at their respective spatial frequencies are included; therefore a single cell can contribute with counts in two different spatial frequencies. Note that this makes the proportions between flows and gratings at each SF different than those in Fig. 1D, since there we considered the spatial frequency of the stimulus with highest firing rate (among the multiple significant ones). Total counts at 0.04, 0.15, 0.24, 0.7, 1.0, 1.25, and 1.6 cpd, respectively: 0, 162, 100, 91, 56, 33, 41 (flows); 301, 35, 40, 57, 12, 4, 8 (gratings).

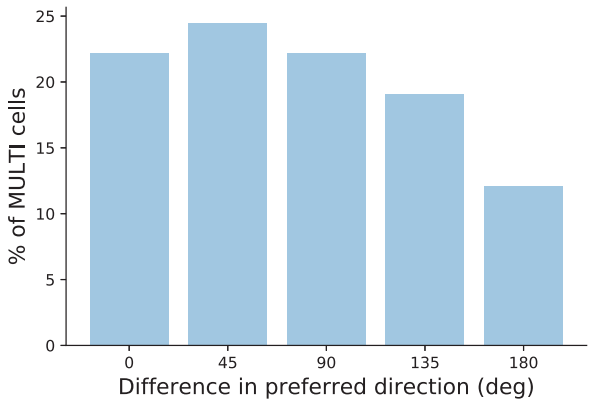

Fig. S18. Distribution of differences in direction preference across stimulus class (flows $vs.$ gratings) for MULTI cells. The difference is computed as the absolute difference in angle between the directions of maximum response for the two stimuli. Although small values predominate, differences as big as 180 degrees are not rare.

References

1. Niell CM, Stryker MP (2008) Highly selective receptive fields in mouse visual cortex. *J Neurosci* 28(30):7520–7536.
2. Niell CM, Stryker MP (2010) Modulation of visual responses by behavioral state in mouse visual cortex. *Neuron* 65(4):472–479.
3. Du J, Blanche TJ, Harrison RR, Lester HA, Masmanidis SC (2011) Multiplexed, high density electrophysiology with nanofabricated neural probes. *PLoS One* 6(10):e26204.
4. Chung JE, et al. (2017) A fully automated approach to spike sorting. *Neuron* 95(6):1381–1394.
5. Swadlow HA (2003) Fast-spike interneurons and feedforward inhibition in awake sensory neocortex. *Cerebral Cortex* 13(1):25–32.
6. Dadarlat MC, Stryker MP (2017) Locomotion enhances neural encoding of visual stimuli in mouse V1. *J Neurosci* 37(14):3764–3775.
7. Shimazaki H, Shinomoto S (2007) A method for selecting the bin size of a time histogram. *Neural Computation* 19(6):1503–1527.